Acoustic modes of finite length homogeneous and layered cylindrical shells: Single and multiwall carbon nanotubes

Guangyan Li, G. A. Lamberton, Jr.,[a] and J. R. Gladden[b]
Department of Physics and Astronomy, University of Mississippi, University, Mississippi 38677, USA

(Received 19 December 2007; accepted 6 June 2008; published online 6 August 2008)

We present a numerical study of the normal modes of vibration of both homogeneous and heterogeneous finite length cylindrical shells of arbitrary wall thickness with applications toward single and multiwall carbon nanotubes in the continuum limit. The method is checked by comparison of computed and measured resonance spectra for a machined aluminum cylindrical shell. The dependence of the natural frequencies of various radial modes with the length and radius of single wall tubes is investigated and compared to atomistic models and Raman spectroscopy data. The radial dependence for the radial breathing mode and four harmonics of the squash mode are found to be well fitted by power laws and agree with analytical solutions in the thin wall limit. A general model for an elastically heterogeneous layered cylindrical shell is applied to multiwall tubes with graphene sheets and gaps between the sheets represented by two different materials. The frequency dependence on length and diameter is investigated for tubes composed of two to four concentric shells. © *2008 American Institute of Physics*. [DOI: 10.1063/1.2965187]

I. INTRODUCTION

Since their discovery in 1991, carbon nanotubes (CNTs) have generated an astounding volume of research.[1] The interest is driven by a unique confluence of a theoretically accessible system with enormous potential for both nanoscale electromagnetic and mechanical applications as well as macroscopic applications such as strong and lightweight composite materials. One aspect of CNTs that has received considerable attention is the various vibrational modes. Certain vibrational modes can be experimentally explored with Raman and IR spectroscopies providing measurements with which to validate theoretical models. Both atomistic and continuum approaches have been used to model vibrational modes of CNTs with infinite and finite lengths.[2–6] Atomistic methods typically use force constant models or density functional theory and are capable of producing reliable results for phonon modes in both the acoustic as well as optical branches. Atomistic methods, however, become costly as the system size increases, a particular problem for multiwall nanotubes (MWNTs). Continuum methods assume that the atomic lattice is "smeared" out to form an equivalent elastic material. Elastic beam theory has been used to explore low frequency bending modes as well as pure radial modes with some success and are easily extended to large systems.[6–8]

This paper presents a different continuum approach to CNT vibrations based on a Rayleigh–Ritz method applied to classic anisotropic elasticity theory. This method is essentially the same one employed by the experimental method of determining the elastic stiffness tensor of a single crystal using resonant ultrasound spectroscopy (RUS) and has also been used in the analysis of oscillations in solid cylindrical fuses.[9–14] The theoretical basis for the calculations, along with modifications suitable for analysis of cylindrical shells, will be reviewed in Sec. II; however, seminal papers first developing the technique can be found in the literature[9,10] along with reviews of RUS in general.[11,12] A few attractive features of this method are as follows: the fully three-dimensional (3D) normal modes are computed (displacements and frequencies), independence of length scales, extensions to different geometries, and even heterogeneous materials is rather straightforward, and computational costs are very low. Computing the first 50 modes of a tube requires about 1 min on a typical desktop computer. We now apply the method to single wall nanotubes as a homogeneous elastic shell of finite length and MWNTs as a heterogeneous layered cylindrical shell.

II. CONTINUUM MODEL

For an elastic solid to exhibit a normal mode, the displacement of each point in that solid must deviate from its rest (unstrained) position with a harmonic time dependence, $\vec{\psi}(\vec{r},t)=\vec{\psi}(\vec{r})\exp\{i\omega t\}$, where $\vec{\psi}$ is the displacement field. By assuming linear elasticity theory, and thus small strains, we may use Hooke's law and Newton's second law to obtain a Lagrangian of the form

$$L=\frac{1}{2}\int\int\int\left(\rho\omega^2\psi_i\psi_i-c_{ijkl}\frac{\partial\psi_i}{\partial x_j}\frac{\partial\psi_k}{\partial x_l}\right)dV, \tag{1}$$

where ρ is the mass density, c_{ijkl} is the elastic stiffness tensor, and the integrand is summed over the directional indices (i,j,k,l), which each range from 1 to 3.

Following the Rayleigh–Ritz procedure, we chose a basis in which to expand the displacement field $\vec{\psi}$. While an orthonormal basis, such as Bessel functions or Legendre polynomials, is an obvious choice since it affords a much simplified analytical approach,[9] a numerical approach allows for many more terms in the expansion. A more general basis

[a]Present address: Materials and Processes Engineering, General Electric Company, Schenectady, New York 12345, USA.
[b]Electronic mail: jgladden@phy.olemiss.edu.

set was proposed by Visscher *et al.*,[10] which expands the displacement in simple powers of the coordinates x, y, and z in the form

$$\psi_i = \sum_{m=1}^{N} a_{mi}\Phi_m, \tag{2}$$

where

$$\Phi_m = \left(\frac{x}{a}\right)^p \left(\frac{y}{b}\right)^q \left(\frac{z}{c}\right)^r,$$

where a, b, and c are related to the dimensions of the resonator—for a cylinder, $a=b=$outer radius and $c=$half the length.[10] The index $m=\{p,q,r\}$ represents a set of three nonnegative integers corresponding to the powers of x, y, and z, and $p+q+r \leq N$ is the cut off condition for the expansion. On a typical desktop computer, machine precision errors begin to accumulate for $N \geq 14$. In all calculations presented here, $N=13$. Such an expansion obviously requires a large number of terms; however, high order polynomials are very flexible functions, which can mimic a wide variety of geometries and displacement fields. A further benefit of an expansion of this form is that integrals and derivatives of this function have the same functional form, only changing the coefficients and powers in a simple way.

Now, by applying the expansion to the Lagrangian and minimizing by taking a derivative with respect to the expansion coefficients, we may cast the problem into the form of an eigenvalue problem,

$$\Gamma_{minj} d_{nj} = \omega^2 E_{minj} d_{nj}, \tag{3}$$

where

$$E_{minj} = \delta_{ij} \int\int\int \rho \Phi_m \Phi_n dV$$

and

$$\Gamma_{minj} = \int\int\int c_{ijkl} \frac{\partial \Phi_m}{\partial x_k} \frac{\partial \Phi_n}{\partial x_l} dV,$$

where the frequencies of the normal modes can be computed from the eigenvalues ($\omega = 2\pi f$), and $\mathbf{d}$ contains the expansion coefficients for the terms in the expansion basis, which can later be used to compute surface displacements.

The elements for the potential energy matrix $\mathbf{\Gamma}$ and kinetic energy $\mathbf{E}$ require the evaluation of the volume integrals, which we denote by $\mathbf{F}$, and are functions of the exponents (p,q,r): $\Gamma_{minj} = c_{ijkl} F_{mknl}$, where summation over repeated indices is understood and the indices m and n represent sets of the exponents $\{p,q,r\}$, as noted above. From this point, we shall drop the indices for the $\mathbf{F}$ matrix and related matrices for brevity. As stated above, all the volume integrals will have a similar form with limits $(-1:1)$ due to the normalized coordinates. For a cylindrical shell, we must also incorporate the inner radius (r_i) of the shell in a normalized fashion, so we define the dimensionless parameter $\alpha = r_i / r_o$. The volume integrals of the shell can then be evaluated by integrating over a full cylinder and subtracting off the empty core,

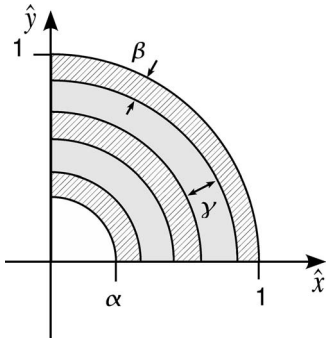

FIG. 1. Model for a heterogeneous cylindrical shell in normalized coordinates viewed along the shell axis (only one-quarter of the cross section is depicted). The hatched regions represent material A (three layers) and shaded regions represent material B (two layers). The geometric parameters α, β, and γ represent normalized complete wall and layer thicknesses, respectively.

$$F = F_{\text{full}} - F_{\text{core}}, \tag{4}$$

where

$$F_{\text{full}} = \int_{-1}^{1} z^r dz \int_{-1}^{1} x^p dx \int_{-\sqrt{1-x^2}}^{\sqrt{1-x^2}} y^q dy,$$

$$F_{\text{core}} = \int_{-1}^{1} z^r dz \int_{-1}^{1} x^p dx \int_{-\sqrt{\alpha-x^2}}^{\sqrt{\alpha-x^2}} y^q dy.$$

An evaluation of the above integrals yields a function of the form

$$F = (1 - \alpha^{(p+q+2)}) 4\pi \frac{(p-1)!!\,(q-1)!!}{(r+1)(p+q+2)!!}, \tag{5}$$

which is also valid for a solid cylinder if $\alpha=0$. The double factorial is defined by $n!! = n \times (n-2) \times \cdots \times 3 \times 1$ for n odd with the product ending in $\cdots \times 4 \times 2$ for n even and $-1!!=0!!=1$ by definition. It should be noted that for very thin shells ($\alpha > 0.90$), the numerical scheme becomes unstable. We expect that by changing the basis to one more naturally suited for a cylindrical geometry, this limit could be improved. In the regime for which the numerics are stable, however, the xyz basis does produce reliable results (see Sec. III).

To model an elastically heterogeneous material such as a cylindrical shell composed of alternating layers of different materials (A and B), one can follow a similar procedure. The volume that was subtracted above to generate the core (F_{core}) of the shell can be extended to subtract out layers in the wall of the cylinder. These gaps can then be replaced by a material with different mechanical properties. The elements in Γ then become $\Gamma = cF + (c' - c)G$, where F is previous volume integral, G represents the integrals over the volume occupied by the material B , c are the elastic parameters for material A, and c' are those for material B. All layer thicknesses are normalized with respect to the outer radius of the shell: $\alpha = r_i / r_o$ (as before), $\beta = t_A / r_o$, and $\gamma = t_B / r_o$, where t_A and t_B are the thicknesses of the layers of materials A and B, respectively. These parameters are shown in Fig. 1.

We now consider a system composed of n layers of material A and $n-1$ layers of material B (Fig. 1 shows the n

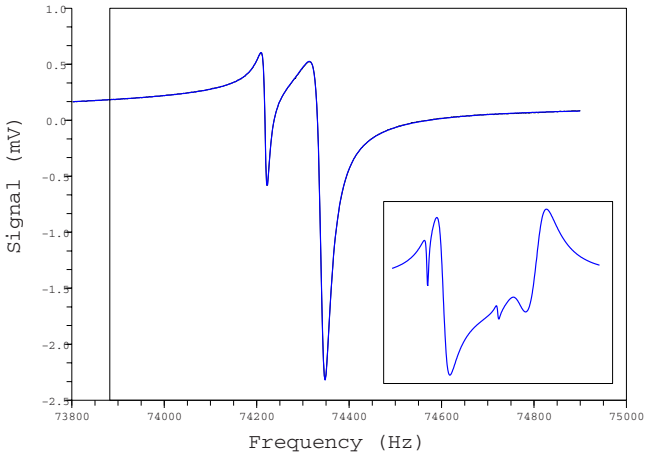

FIG. 2. (Color online) Raw resonance data and fits for modes 20 and 21. The signal to noise ratio is so high that the fit curve and data are indistinguishable in the plot. The single frequency derived from these data is an amplitude weighted average of the two peaks (74.305 KHz in this case). The inset shows the five peaks for modes 3–7. Although the fit to the raw data is quite good, these peaks were excluded from the spectrum fit because of the many strongly overlapping peaks.

$=3$ case). Then the normalized inner radius can be expressed in terms of the layer thicknesses: $\alpha=1-2nt_A-2(n-1)t_B$. The G integrals then take the form

$$G=\frac{8}{r+1}\sum_{i=1}^{n-1}\left[\int_0^{U+\gamma}dx\int_0^{\sqrt{(U+\gamma)^2-x^2}}dyx^py^q-\int_0^{U}dx\int_0^{\sqrt{U^2-x^2}}dyx^py^q\right]$$
$$=4\pi\frac{(p-1)!!(q-1)!!}{(n+1)(p+q+2)!!}\sum_{i=1}^{n-1}[(U+\gamma)^{p+q+2}-U^{p+q+2}], \quad (6)$$

where $U=1-(n-i)(\beta+\gamma)$. The z integrals have already been performed by exploiting the symmetry of the intervals to produce the coefficient $8/(r+1)$. Numerically, the values of F and G can be precomputed and stored in arrays with appropriate elements called to evaluate each element in the Γ matrix. Once the matrices are populated, the eigenvectors and eigenvalues can be computed. The eigenvectors are the set of coefficients for each term in expansion basis from which displacements for each mode can be reconstructed and eigenvalues are the resonance frequencies.

III. EXPERIMENTAL VERIFICATION

The model for the homogeneous shell was tested by performing a RUS type of experiment in which an aluminum shell was machined with a precise geometry using a wire electric discharge machine. The dimensions of the shell are $L=4.93$, outer diameter$=1.93$, and inner diameter$=1.26$ cm. so $\alpha=0.65$. The resonance spectra were measured using a set of transducers, an SRS DS 345 synthesizer to drive the system, and an SRS SR844 lock-in amplifier to monitor the response of the shell. Some sample data are shown in Fig. 2. The x-y symmetry of the cylinder generates many doublets. For a real resonator, slight geometric errors result in a splitting of the doublets, as shown in Fig. 2. The resonance peaks are fitted with a Bright–Wigner line shape (Lorentzian with an arbitrary phase factor), so the center frequency and quality factor can be extracted. For comparison to computed frequencies, single valued doublets are generated by taking an average of the frequencies weighted by the amplitude of the peaks. The elastic parameters were adjusted slightly to minimize the sum of the errors, as one might do in a typical RUS experiment. Table I lists a comparison of the measured spectra, which are also computed with the following parameters: dimensions unchanged, Young's modulus $E=69.4$ GPa, and Poisson's ratio $\sigma=0.252$, and using the highest polynomial order $N=13$. Modes 3–7 were not given any weight when minimizing the error because those modes were all closely spaced and strongly overlapping (see Fig. 2 inset). The eigenvectors were used to generate surface displacement plots for each of the normal modes (see Fig. 3).

TABLE I. Measured and computed natural frequencies in MHz of the cylindrical aluminum shell. Modes 3–7 (denoted with †) were excluded in the fit to the spectrum (see Fig. 2 inset).

Mode	f_{expt}	f_{calc}	|% err|
1	0.029 098	0.028 850	0.86
2	0.029 098	0.028 850	0.86
3†	0.031 792	0.031 249	1.74
4†	0.031 792	0.031 249	1.74
5†	0.032 491	0.032 455	0.11
6†	0.032 919	0.032 501	1.29
7†	0.032 919	0.032 501	1.29
8	0.038 919	0.038 773	0.38
9	0.038 919	0.038 773	0.38
10	0.049 853	0.050 453	1.19
11	0.049 853	0.050 453	1.19
12	0.050 968	0.050 800	0.33
13	0.053 686	0.053 870	0.34
14	0.053 686	0.053 870	0.34
15	0.064 846	0.064 911	0.10
16	0.071 045	0.070 879	0.24
17	0.071 045	0.070 879	0.24
18	0.072 585	0.072 467	0.16
19	0.072 585	0.072 467	0.16
20	0.074 305	0.074 187	0.16
21	0.074 305	0.074 187	0.16
22	0.080 916	0.080 830	0.11
23	0.080 916	0.080 830	0.11
24	0.081 862	0.081 985	0.15
25	0.081 862	0.081 985	0.15

IV. MODELING OF SINGLE WALL NANOTUBES

The computational scheme was verified in Sec. III using a macroscopic sample with length scales on the order of centimeters. However, all length scales are normalized in the model, which allows us to consider resonators of any length scale. We now apply the scheme to a single wall carbon nanotube (SWNT). Nanotubes are particularly amenable to continuum approximations because of the hexagonal symmetry of graphene sheets that compose the walls of the tube. A result from group theory is that hexagonal symmetries are elastically isotropic, meaning that we can describe the stiff-

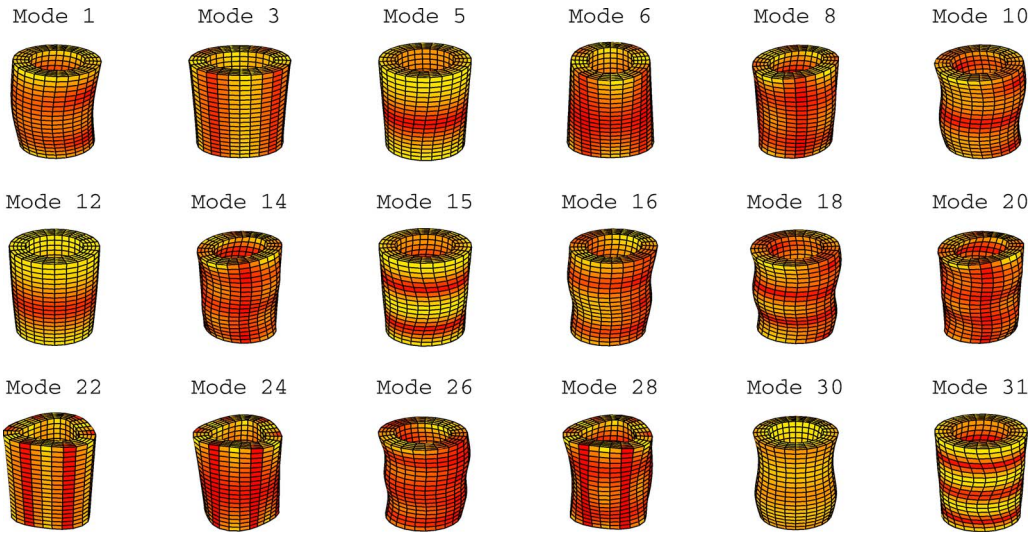

FIG. 3. (Color online) Normal modes of the aluminum cylindrical shell. Darker (red in color) regions denote nodal regions. Skipped numbers indicate degenerate modes due to the symmetry of the cylinder.

ness of the walls of a nanotube simply with a Young's modulus (E) and Poisson's ratio (σ).[15] Values for E and σ for a SWNT have been explored both theoretically and experimentally and vary widely in the literature.[16] As representative values, we choose $E=1.0$ TPa and $\sigma=0.20$. These values correspond to a shear modulus $G=0.42$ TPa. An additional required parameter is the mass density for which we use a value of $\rho=2.26$ g/cm^3. The wall thickness was taken to be the thickness of a single graphene sheet, $t=0.14$ nm, and the OD of the SWNT is computed from the chiral indices of the tube (n,m) in the following way: $d=a\sqrt{3}/\pi\sqrt{n^2+m^2+nm}+t$, where $a=0.144$ nm is the lattice constant of a SWNT.[17]

Nanotubes typically have exceedingly large aspect ratios with lengths on the order of tens to hundreds of microns and diameters on the order of a few nanometers. The normal modes of such a structure will be dominated by one dimensional "wave-on-a-string-type" modes in the lower frequency range. The density of vibrational states increases rapidly with mode number and would become a near continuum of states before any radial modes were excited. To avoid this problem, tubes of finite length and modes independent of length are investigated. To facilitate comparison with results from other groups, we convert the frequencies of all modes to wavenumbers in units of cm^{-1}. Modes which are dominated by radial displacements are of particular interest because they are found to depend on a power law fashion on the diameter of the tube only. This quality makes these modes good markers for diameter selection of a nanotube sample, which will typically have a very wide range of lengths. The wavenumbers of the modes can then be used to determine the diameters of the tubes in the sample.[18] Figure 4(a) depicts the nodeless radial breathing mode (RBM) and Figs. 4(b)–4(e) depict the fundamental squash mode (SM) and the next three higher harmonics of that mode. In standard symmetry notation, the RBM has an A_{1g} symmetry and the SM has an E_{2g} symmetry. The axial view of the RBM in Fig. 4(a), the SM in Fig. 4(b), and the first harmonic of the SM in Fig. 4(c) can be compared to the 3D construction of modes 12, 3, and 22, respectively in Fig. 3.

Our first numerical investigation was the length dependence of the radial modes. The resonance spectra for two armchair tubes of types (8,8) and (12,12) were computed for a range of lengths. Figure 5 shows the wavenumbers for the RBM and SM with increasing length for the 12-12 tube. Both these modes become essentially independent of length once L/d exceeds ~ 2; that is, when the structure becomes more of a geometric tube than a ring. The trends are fitted with scaling functions of the form $\omega=a+b(L/d)^c$, with a being the asymptotic wavenumber for an infinitely long tube. The fitted exponents were $c_{\mathrm{RBM}}=-2.98$ and $c_{\mathrm{squash}}=-0.655$ and asymptotes were $a_{\mathrm{RBM}}=135$ cm^{-1} and $a_{\mathrm{squash}}=18.0$ cm^{-1}. These values can be compared to the force constant calculations of Kahn and Lu[2] of 131 and 11 cm^{-1},

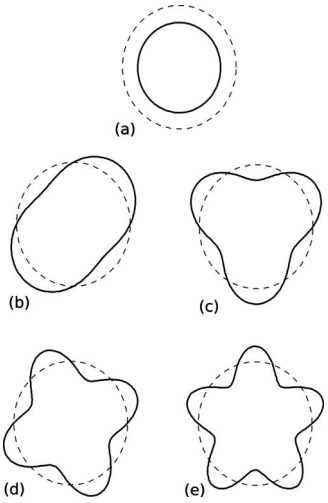

FIG. 4. Azimuthal displacements for length independent modes. The dashed circle represents the undisplaced cylinder walls for reference. (a) is the RBM, (b) is the fundamental SM, and (c)–(e) are the higher harmonics of the SM.

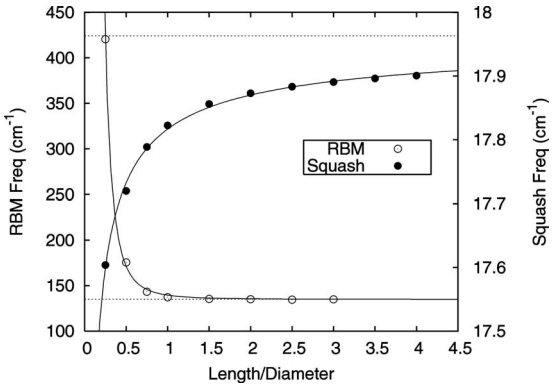

FIG. 5. Wavenumber of the RBM and SM of a $(n,m)=(12,12)$ SWNT as the length to diameter ratio is increased. The solid lines are fits of the data to power laws with parameters reported in the text and dashed lines show the asymptotic values for large values of L/d.

respectively (see Table II). At $L/d=2.0$, the wavenumber for the SM only deviates from its asymptotic value by about 0.5%. For subsequent calculations in which radial dependence is investigated, the length was set to be twice the current diameter to ensure length independence. The calculations for the (8,8) tube showed very similar scaling.

We now turn to the diameter dependence of these modes. By using the SWNT material properties described above, we compute the spectra for a range of discrete diameters arising from the tube indices (n,m) and use the expression for the d described previously. The results for the RBM, SM, and its first three harmonics are shown in Fig. 6. The trends seem to be well described by a power law (solid lines) of the form $k(d)=bd^c$, where the approximate $1/r$ dependence for the RBM and $1/r^2$ dependence for the fundamental SM agrees well with atomistic calculations and is commonly used to measure SWNT diameter distributions from Raman spectroscopy data.[2,3,18] Force constant calculations of the Raman active RBM have demonstrated that the wavenumbers are well fitted by $k(d)=224$ cm nm$^{-1}/d$ [see dashed line in Fig. 6(a)].[18] Furthermore, that study also found that tubes of all chiralities fell on this universal curve, validating our assumption that the walls are elastically isotropic. Our value for the coefficient of 259 cm^{-1} shows reasonable agreement and

TABLE II. Wavenumbers in cm^{-1} for the length independent RBM and SM of a SWNT over a range of diameters and tube types designated by the tube indices (n,m). The diameters (d) listed are slightly higher than are typically reported because we add an effective wall thickness (t) based on the thickness of the graphene layer (see text). Our continuum limit results are compared to the atomistic results of Kahn and Lu. (Ref. 2).

Type d (nm)		This work Squash	RBM	Kahn and Lu Squash	RBM
(12,0)	1.09	52	234	33	226
(8,8)	1.24	39	203	25	197
(9,9)	1.38	31	180	20	175
(16,0)	1.41	29	176	19	170
(10,10)	1.52	26	162	16	157
(18,0)	1.57	24	156	15	151
(11,11)	1.65	21	147	13	143
(12,12)	1.79	18	135	11	131

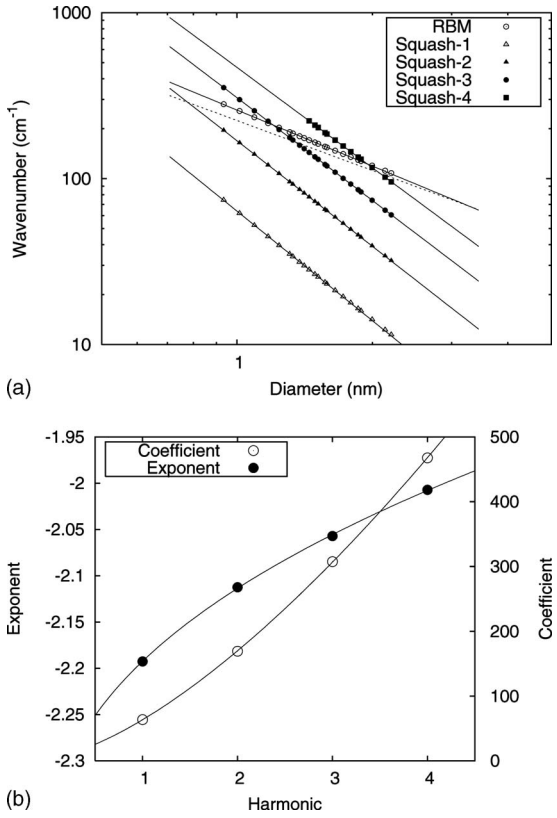

FIG. 6. (a) Radial dependence of four length independent modes plotted in log-log scale. The solid lines are power law fits and the dashed line is a power law obtained by Bandow *et al.* (Ref. 18). The numbers following the squash labels in the legend correspond to the harmonics of that mode. (b) Fit parameters for the power laws presenting the solid lines in the upper plot.

could probably be improved by tuning the elastic parameters. It is perhaps not surprising that our continuum model deviates from the atomistic calculations most sharply for the smallest diameter tubes, which have the smallest number of atoms and the highest curvature.

Recent analytical progress on normal modes of elastic tubes in the limit of thin walls has been made by Mahan.[19] Mahan derived a frequency expression for a set of modes in which the "entire tube oscillates sinusoidally" along the circumference, which we take for our SM and its higher harmonics. In terms of the frequency of the RBM (ω_{RBM}), the analytical solution for the SM frequencies in the thin wall limit is

$$\omega_{\mathrm{SM}_n} = \omega_{\mathrm{RBM}} \frac{h}{\sqrt{3}a} \frac{n(n^2-1)}{\sqrt{n^2+1}}, \tag{7}$$

where h is the wall thickness, a is the tube radius, and n is the number of azimuthal nodal points for the harmonic. Figures 4(b)–4(e) show these modes for $n=4,6,8$, and 10, respectively. Our numerical results show good agreement with Mahan's[19] analytical solution with the largest deviation occurring for the smallest diameter tubes, in which the thin wall limit is less applicable (see Fig. 7).

V. MODELING OF MULTIWALL NANOTUBES

Section II describes a scheme for computing the normal modes of a heterogeneous layered cylindrical shell. We now

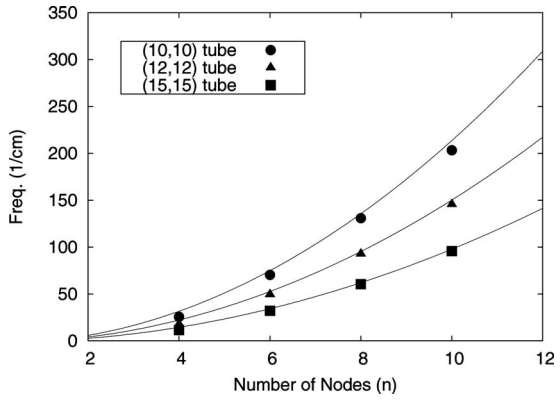

FIG. 7. Wavenumber for the SM harmonics as a function of a number of nodes [see Figs. 4(b)–4(e)]. The solid lines are analytical solutions (not fits) from Mahan (Ref. 19), which assume a thin wall. Note that agreement is best for the larger diameter tubes for which the wall thickness to tube diameter ratio is smallest.

apply that scheme to a MWNT. We take material A to form the concentric walls of the tubes containing the rolled graphene layers. These layers will thus have the same material properties for a single wall tube described in Sec. IV and the wall thickness $t_A=t=0.144$ nm. Material B will form the gaps between the walls of the tube and will thus have elastic parameters related to the interlayer bonding between tube walls. For the wall thickness (t_B) we take a typical interwall spacing of 0.34 nm.[6] We take the elastic constant $c_{33}=36.5$ GPa of graphite to reasonably estimate the effective Young's modulus of the gap.[20] This weak interlayer bonding is why graphite makes a good dry lubricant and contributes to the ease with which the walls of a MWNT can slide axially or "telescope," although registry mismatch between layers also plays a significant role.[21] This strong anisotropy between the intralayer and interlayer bonding has prompted other researchers to explore whether the walls in a MWNT essentially resonate independently of one another or if the entire structure resonates as a cohesive unit.[6,7] Atomistic approaches to MWNT dynamics are often limited by the computational cost as each new wall adds many new atoms to compute.[6] Adding layers in our continuum model, however, comes at a small computational cost with resonance spectra typically computed at the order of 1 min.

Just as with the single wall tubes, we first check what the minimum length of the MWNT must be before the resonance becomes independent of length. We find that the MWNTs exhibit a similar response to the SWNTs and that length independence is achieved with a length at least twice the diameter. The inset in Fig. 8 shows the RBM for a double wall nanotube (DWNT) with indices (18,18) for the outer tube. The solid curve is a fit to $k=a+b(L/d)^c$ with $a=91.0$ cm^{-1}, $c=-3.9$, and $b=0.4$ cm^{-1}. We see here that the roughly inverse cubic trend exhibited by the thinner walled SWNTs for this mode (see above) now falls off even more quickly and roughly as the inverse quartic. All radial dependence calculations were performed with $L/d=2.0$.

The radial dependence (Table III) of the RBM for tubes consisting of one to four walls is shown in Fig. 8(a). The trends are again well fitted with power laws. Also plotted are some results from Popov and Henrard[6] for a double wall

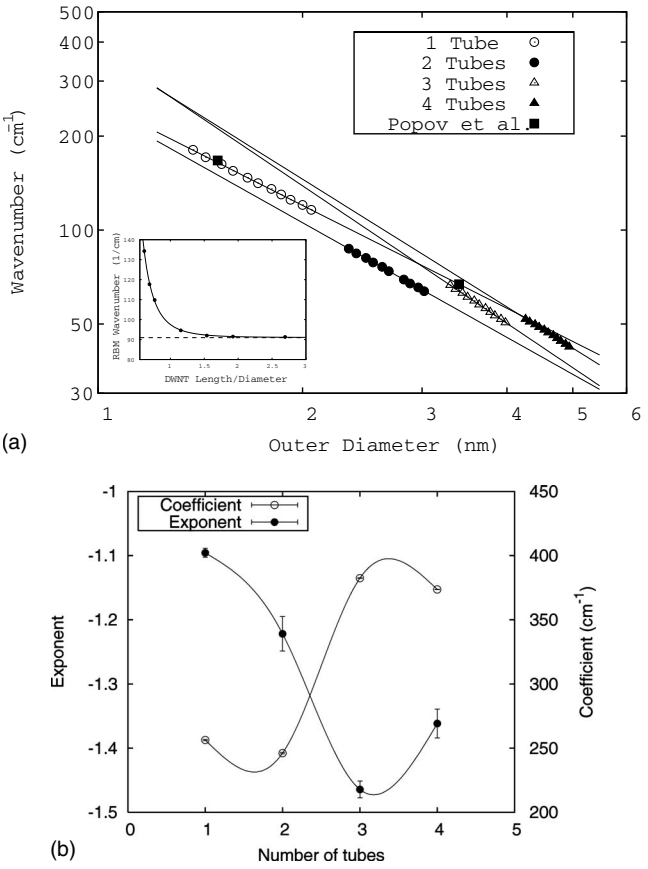

FIG. 8. RBM for a multiwall tube consisting of one to four tubes. (a) The radial dependence of the wavenumber for the RBM plotted using a log-log scale. The square points are results from Popov and Henrard (Ref. 6) and are discussed in the text. The inset shows the RBM wavenumber for a DWNT tube with a (18,18) outer tube as its length is increased. Calculations for (a) were made with $L/d=2$ The solid lines are power law fits and (b) plots the power law fit parameters as a function of the number of tubes. The solid lines in (b) are cubic splines to guide the eyes.

tube. They listed separate frequencies for the inner and outer tubes, suggesting independent resonances. The points plotted are for the outer tube and fall precisely on our scaling curve for a single wall tube of equal diameter. Figure 8(b) plots the coefficient and exponents from the fits as the number of tubes is varied. We see here a nonmonotonic trend (solid lines are cubic splines) with a maximum magnitude of about $-\frac{3}{2}$ for the exponent and coefficient occurring for the MWNT with three walls. The corresponding plots for the SM are shown in Fig. 9. The exponent for the SM shows a stronger dependence on the number of walls in the tube, transitioning from the approximate $1/d^2$ behavior for the single tube toward $1/d^3$ as the number of tubes increases. Also interesting

TABLE III. Power law coefficients and exponents for the radial dependence of the wavenumber for the radial modes depicted in Fig. 4.

Mode type	Coefficient	Exponent
RBM	259.0	−1.12
Squash 1	63.7	−2.19
Squash 2	169.2	−2.11
Squash 3	307.5	−2.06
Squash 4	467.8	−2.01

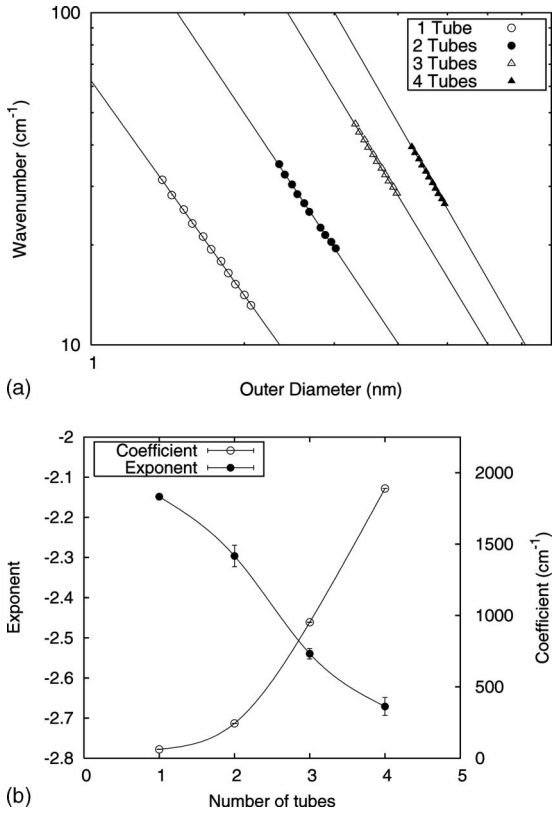

FIG. 9. SM for a multiwall tube consisting of one to four tubes. (a) The radial dependence of the wavenumber for the SM plotted using a log-log scale. The solid lines are power law fits and (b) plots the power law fit parameters as a function of the number of tubes. The solid lines in (b) are cubic splines to guide the eye.

to note is the strong dependence of the coefficient, increasing by a factor of almost 30 as the number of walls increases from 1 to 4.

VI. SUMMARY

We have applied an elastic continuum model to explore various normal modes of vibration of both SWNTs and MWNTs. The model is an extension to the theory used in a RUS measurement in which the fully 3D normal modes of an elastic solid are computed. An important benefit from this method over other continuum models is that (i) thin-beam-like geometries are not required as in Euler–Bernoulli and Timoshenko methods and (ii) nonaxisymmetric modes can be explored. The character of the nonradial modes of finite length tubes will become important as applications of CNTs in microelectromechanical systems increases. Atomistic models, however, do provide insight into individual atom motions and higher frequency optical band phonon modes.

Our study of the RBM and SM shows the well documented $1/d$ and $1/d^2$ dependences of the frequency, respectively. We also explore the diameter trends for several higher harmonics of the SM and find a systematic decrease in the magnitude of the exponent by about 10% from the first to fourth harmonics (2.2–2.0). Our investigations of MWNTs showed wavenumbers for RBM and SM well fitted by power laws with exponents dependent on the number of walls. The RBM for the MWNT exhibits a nonmonotonic shift in the exponent with an increasing number of walls, in contrast to the SM, which shows a steady increase in the exponent magnitude.

ACKNOWLEDGMENTS

We would like to thank Professor J. D. Maynard of The Pennsylvania State University for assistance with the cylinder shell code, the University of Mississippi for its support of this project, and Micheal Reep for machining the aluminum cylinder. This work was also supported by the Department of Energy EPSCoR Award No. DE-FG02-04ER46121.

[1] S. Iijima, Nature (London) **354**, 56 (1991).
[2] D. Kahn and J. P. Lu, Phys. Rev. B **60**, 6535 (1999).
[3] A. M. Rao, E Richter, S. Bandow, B. Chase, P. C. Eklund, K. A. Williams, S. Fang, K. R. Subbaswamy, M. Menon, A. Thess, R. E. Smalley, G. Dresselhaus, and M. S. Dresselhaud, Science **275**, 187 (1997).
[4] T. Yumura, D. Nozaki, S. Bandow, K. Yoshizawa, and S. Iijima, J. Am. Chem. Soc. **127**, 11769 (2005).
[5] Y. Liu, R. O. Jones, X. Zhao, and Y. Ando, Phys. Rev. B **68**, 125413 (2003).
[6] V. N. Popov and L. Henrard, Phys. Rev. B **65**, 235415 (2002).
[7] J. M. Benoit, J. P. Buisson, O. Chauvet, C. Godon, and S. Lefrant, Phys. Rev. B **66**, 073417 (2002).
[8] I. R. Fernandez, H. Fangohr, and A. Bhaskar, J. Phys.: Conf. Ser. **26**, 131 (2006).
[9] H. H. Demarest, Jr., J. Acoust. Soc. Am. **49**, 768 (1971).
[10] W. M. Visscher, A. Migliori, T. Bell, and R. Reinert, J. Acoust. Soc. Am. **90**, 2154 (1991).
[11] J. D. Maynard, Phys. Today **49**, 26 (1996).
[12] A. Migliori, J. L. Sarrao, W. M. Visscher, T. M. Bell, M. Lei, Z. Fisk, and R. G. Leisure, Physica B (Amsterdam) **183**, 1 (1993).
[13] A. Migliori and J. Sarrao, *Resonant Ultrasound Spectroscopy* (Wiley, New York, 1997).
[14] G. D. Mahan, J. R. Gladden, and J. D. Maynard, J. Appl. Phys. **90**, 4415 (2001).
[15] A. E. H. Love, *A Treatise on the Mathematical Theory of Elasticity* (Dover, New York, 1944), Sec. 334, p. 545.
[16] A. Zettl and J. Cumings, in *Handbook of Elastic Properties of Solids, Liquids, and Gases*, Elastic Properties of Solids: Theory, Elements and Compounds, Novel Materials, Technological Materials, Alloys, and Building Materials Vol. II, edited by M. Levy, H. Bass, and R. Stern (Academic, New York, 2001), Chap. 11.
[17] R. Saito, G. Dresselhaus, and M. S. Dresselhaus, *Physical Properties of Carbon Nanotubes* (Imperial College, London, 1999).
[18] S. Bandow, S. Asaka, Y. Saito, A. M. Rao, L. Grigorian, E. Richter, and P. C. Eklund, Phys. Rev. Lett. **80**, 3779 (1998).
[19] G. D. Mahan, Phys. Rev. B **65**, 235402 (2002).
[20] A. A. Ahmadieh and H. A. Rafizadeh, Phys. Rev. B **7**, 4527 (1973).
[21] J. Cumings and A. Zettl, Science **289**, 602 (2000).